2D and 3D Ruthenium Nanoparticle Covalent Assemblies for Phenyl Acetylene Hydrogenation

Yuanyuan Min, Faqiang Leng, Bruno F Machado, Pierre Lecante, Pierre Roblin, Hervé Martinez, Thomas Theussl, Alberto Casu, Andrea Falqui, María Barcenilla, et al.

2D and 3D Ruthenium Nanoparticle Covalent Assemblies for Phenyl Acetylene Hydrogenation

Yuanyuan Min,[a] Faqiang Leng,[a] Bruno F. Machado,[b] Pierre Lecante,[c] Pierre. Roblin,[d] Hervé Martinez,[e] Thomas Theussl,[f] Alberto Casu,[g] Andrea Falqui,[g] María Barcenilla,[h] Silverio Coco,[h] Beatriz María Illescas Martínez,[i,j] Nazario Martin,[i,j] M. Rosa Axet,*[a] and Philippe Serp*[a]

Abstract: The bottom-up covalent assembly of metallic nanoparticles (NP) represents one of the innovative tools in nanotechnology to build functional heterostructures, with the resulting assemblies showing superior collective properties over the individual NP for a broad range of applications. The ability to control the dimensionality of the assembly is one of the major challenges in designing and understanding these advanced materials. Here, two new organic linkers were used as building blocks in order to guide the organization of Ru NP into two- or three-dimensional covalent assemblies. The use of a hexa-adduct functionalized C_{60} leads to the formation of 3D networks of 2.2 nm Ru NP presenting an interparticle distance of 3.0 nm, and the use of a planar carboxylic acid triphenylene derivative allows the synthesis of 2D networks of 1.9 nm Ru NP with an interparticle distance of 3.1 nm. The Ru NP networks were found to be active catalysts for the selective hydrogenation of phenylacetylene, reaching good selectivity toward styrene. Overall, we demonstrated that catalyst performances are significantly affected by the dimensionality (2D vs. 3D) of the heterostructures, which can be rationalize based on confinement effects.

1. Introduction

Catalysts are essential in the majority of industrial chemical transformation processes, and the optimization of catalyst performances is a *sine qua non* condition for a sustainable industrial development. In nature, the chemical transformation processes often occur in molecularly crowded and/or confined environment with well-designed limited spaces such as nanometric-sized enzymes.[1] With the development of nanosciences and nanotechnology, various nanoreactors, both organic or inorganic,[2] have been designed for catalytic applications;[3] providing constrained spaces isolated from the surrounding environment. In heterogeneous catalysis, confinement effects (CE) can greatly influence catalytic performances.[4] The CE can be either physical or chemical, and are induced by the reduction of the dimensions of the spaces in which a chemical reaction takes places. The physical effects can lead to shape-selectivity,[5] impact the nanofluidics and mass transport,[6] phase separation,

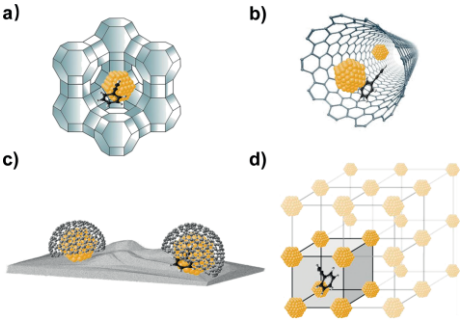

Scheme 1. Representation of different nanoreactors with a confined metallic nanoparticle and a reactant molecule (here phenyl acetylene): a) a metallic cluster confined in a zeolite cage; b) metallic clusters confined in a carbon nanotube; c) metallic clusters covered by a graphene overlayer; and d) covalent network of metallic clusters where the black lines represent the organic linkers.

[a] *Dr. Y. Min, Dr. F. Leng, Dr. M. Rosa Axet, Prof. Dr. P. Serp*
CNRS, LCC (Laboratoire de Chimie de Coordination),
INPT, 205 route de Narbonne, 31077 Toulouse Cedex 4, France
E-mail: rosa.axet@lcc-toulouse.fr, philippe.serp@ensiacet.fr
https://www.lcc-toulouse.fr/article447.html?lang=fr
Twitter: Laboratoire de chimie de coordination @LCC_CNRS

[b] *Dr. B. F. Machado*
LSRE-LCM, Chemical Engineering Department, Faculty of Engineering, University of Porto, Rua Dr. Roberto Frias s/n, 4200-465 Porto, Portugal

[c] *Dr. P. Lecante*
Centre d'élaboration des matériaux et d'études structurales UPR CNRS 8011, 29 Rue Jeanne-Marvig, BP 4347, 31055 Toulouse, France

[d] *Dr. P. Roblin*
Laboratoire de Génie Chimique and Fédération de Recherche FERMAT, 4 allée Emile Monso, 31030 Toulouse, France

[e] *Prof. Dr. H. Martinez*
Université de Pau et des Pays de l'Adour, 64053 Pau, France

[f] *Dr. T. Theussl*
King Abdullah University of Science and Technology (KAUST), Visualization Core Lab, 23955-6900 Thuwal, Saudi Arabia

[g] *Dr. A. Casu, Dr. A. Falqui*
King Abdullah University of Science and Technology (KAUST), Biological and Environmental Sciences and Engineering (BESE) Division, NABLA Lab, 23955-6900 Thuwal, Saudi Arabia

[h] *Dr. M. Barcenilla, Prof. Dr. S. Coco*
IU CINQUIMA/Química Inorgánica, Facultad de Ciencias, Universidad de Valladolid, 47071 Valladolid, Spain

[i] *Prof. Dr. B. M. I. Martínez, Prof. Dr. N. Martin*
Departamento Química Orgánica, Facultad C. C. Químicas, Universidad Complutense de Madrid, Av. Complutense s/n, 28040 Madrid, Spain

[j] *Prof. Dr. B. M. I. Martínez, Prof. Dr. N. Martin*
IMDEA-Nanociencia, C/Faraday 9, Ciudad Universitaria de Cantoblanco, 28049 Madrid, Spain

Supporting information and ORCID(s) from the author(s) for this article are available on the WWW under https://doi.org/10.1002/ejic.202000698.

Part of the Supported Catalysts Special Collection.

phase equilibria[7] and transformation,[8] or to significant pressure enhancement.[9] The chemical effects are related to modifications of the electronic interactions between the catalytic phase and the surrounding material, which alter the adsorption energetics, influencing the formation and breaking of chemical bonds. All these effects can directly contribute to enhancement of activity/selectivity and catalyst stabilization. CE have been studied in 0D nanoreactors such as zeolites[10] (Scheme 1a) or MOF,[11] 1D nanoreactors such as carbon nanotubes (Scheme 1b)[12] or covalent organic frameworks,[13] and more recently, under the layers of 2D materials such as graphene (Scheme 1c).[14] In all these systems the active phase, often a transition metal nanoparticle (NP), is confined in a cavity composed of a second material. Another type of material that could offer interesting perspectives to study CE consists in covalent assemblies of metallic NP (Scheme 1d).[15] In these structures, the organic linker (or ligand) plays a fundamental role on constructing the NP network and defining NP chemical environment.[16] In that case, the reactant environment is significantly different since it is composed of an important number of catalytically active NP covalently linked by an organic molecule. The interparticle coupling effect has been demonstrated to significantly influence the optical properties of NP,[17] and is also able to affect their catalytic properties.[18]

Although the covalent assembly of well-defined metal NP could permit to direct substrates, or to create confined spaces in order to produce better catalysts by means of CE, most of the studies dealing with this type of material concentrated on applications for biomedicine electronics or optics,[19] and they are up to now only a limited number of studies dedicated to their use in catalysis.[15a,15b,20] Some studies have already evidenced that NP covalent assembly show better catalytic performances, and in some cases higher stability than isolated NP.[20,21] Another interesting aspect of these assemblies is the possibility of controlling the interparticle distance via the molecular chemical nature and chain length of the ligand,[15a,22] and possibly the CE. We have recently demonstrated in the case of 3D Ru NP networks linked with polymantane ligands that it was possible to: i) obtain NP with similar size (1.6–1.8 nm) for a given metal loading whatever the nature of the ligand (diacid or diamine); ii) control the electronic effects by means of the chemical nature of the ligand (acid vs. amine); and iii) control the interparticle distance via the size of the ligand.[15a] We also demonstrated that catalyst activity and selectivity in phenylacetylene hydrogenation are both significantly affected by Ru NP interparticle distance and therefore by CE.

In continuation of our ongoing research in the development of Ru NP covalent assemblies for catalysis,[15a,15b] the present work aims at producing 2D and 3D Ru NP networks via a rational choice of new organic linkers, and to study their catalytic performances for phenylacetylene hydrogenation. Elucidation of confinement of Ru NP and architecture of the network (2D vs. 3D) on catalyst activity/selectivity is also one of the objectives of the present study.

2. Results and Discussion

In previous works by some of us, 3D Ru NP covalent assemblies with homogeneous interparticle distances have been produced

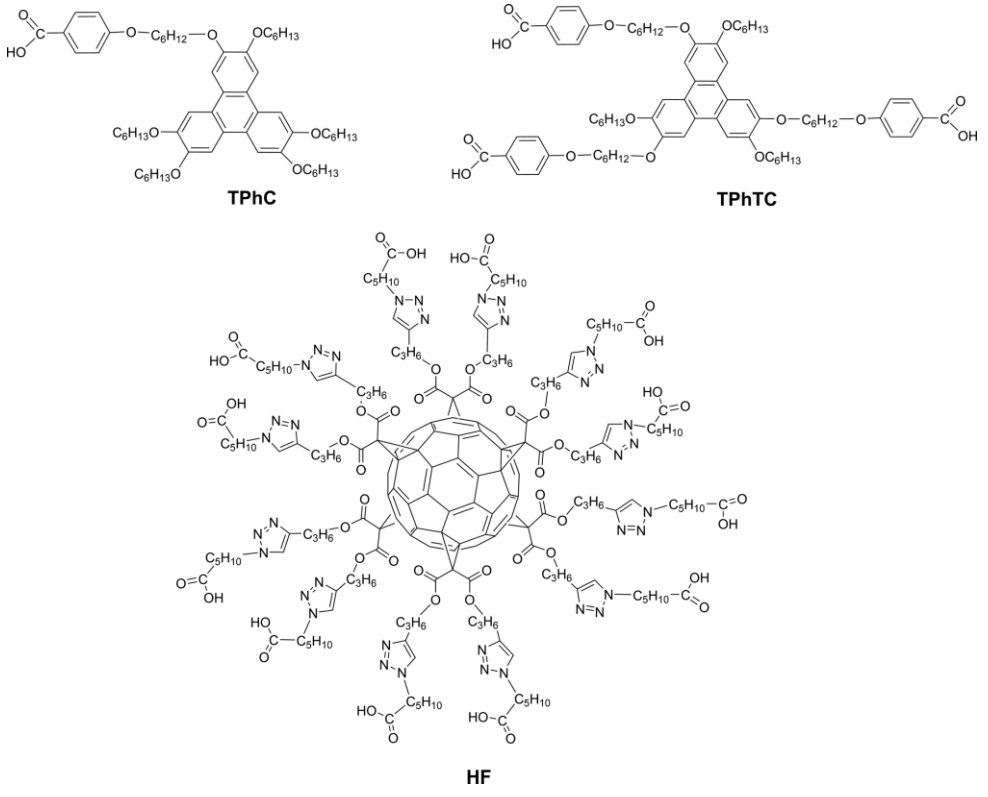

Scheme 2. Carboxylic acid linkers for Ru NP: **TPhC**, **TPhTC** and **HF**.

using spacer molecules such as a multi-adduct fullerene ($C_{66}(COOH)_{12}$)[15b] or di-topic polymantane derivatives.[15a] The distance between the NP is controlled in accordance to the different size of the ligands. Herein, the hexa-adduct functionalized C_{60} (**HF**) ligand (Scheme 2) has been synthesized and employed as tethering ligand for Ru NP in order to investigate the effect of the size of the ligand in opposition to the previously investigated multi-topic $C_{66}(COOH)_{12}$.[15b] Indeed, the intermediary long chains present in **HF** should contribute to increase the interparticle distance. Further, we hypothesized that the use of planar ligands could produce 2D assemblies. Hereof, carboxylic acid triphenylene derivatives depicted in Scheme 2 have been used as NP stabilizers. Both compounds, 2(6-(4-(carboxy)phenoxy)hexyloxy)-3,6,7,10,11-pentakis(hexyloxy)triphenylene (**TPhC**) and 2,6,10-tris(6-(4-(carboxy)phenoxy)hexyloxy)-3,7,11-trihexyloxytriphenylene (**TPhTC**) display the planar triphenylene backbone, and one or three alkyl chains containing each one the carboxylic acid moiety. The molecules possessing substituted triphenylene backbone constitute a classical series of discotic liquid crystal molecules.[23] However, the mono carboxylic acid **TPhC** melts directly to an isotropic liquid and it is not mesomorphic (Figure S1 of SI). In contrast, the tricarboxylic acid derivative **TPhTC** shows an enantiotropic nematic mesophase (N) (from 55 to 113 °C) followed, on cooling, by a glass transition, which is maintained in the second heating (Figure S1 of SI). The nematic mesophase (N) was identified in optical microscopy by its typical Schlieren texture (Figure S2 of SI). We did not use **TPhTC** in the mesomorphic state, but the different thermal behavior of **TPhC** and **TPhTC** reveals their different self-assembly capacity. The extended aromatic sp^2 basal plane and the six substituents with three carboxylic ending groups at the periphery position of the polyaromatic core could lead to extended and stable self-assemblies.[24] It has already been reported that thanks to the aromatic sp^2 basal plane, similar triphenylene hexa-substituted derivatives afforded 2D metal-organic frameworks, which provided significant activity for O_2 electroreduction.[25] Triphenylene liquid crystals have been also studied as materials for surface modification,[26] as stabilizers of nanoparticles[27] and even as template of inorganic mesostructures.[28] To the best of our knowledge, this is the first time that the ligands depicted in Scheme 2 are used for surface stabilization in NP synthesis.

2.1 Synthesis and Characterization of 2D Ru NP Assemblies

Ru NP were synthesized in THF by decomposition of [Ru(η^4-C_8H_{12})(η^6-C_8H_{10})] under 3 bar of H_2 at room temperature in the presence of **TPhC** or **TPhTC** by using the reaction conditions detailed in the experimental section. TEM images of the as-synthesized Ru NP are presented in Figure 1. The use of the monodentate ligand **TPhC** leads to the formation of isolated NP with mean size of 1.7 ± 0.7 nm (Figure 1a and Figure S3a). Differently, the use of the multi-topic compound **TPhTC**, whatever the Ru/**TPhTC** ratio used, leads to the production of assemblies of Ru NP presenting mean diameter below 2 nm (Figure 1b–e). The size of these NP slightly increased with the Ru content. These data are summarized in Table 1 and size histograms are given in Figure S3 of the SI.

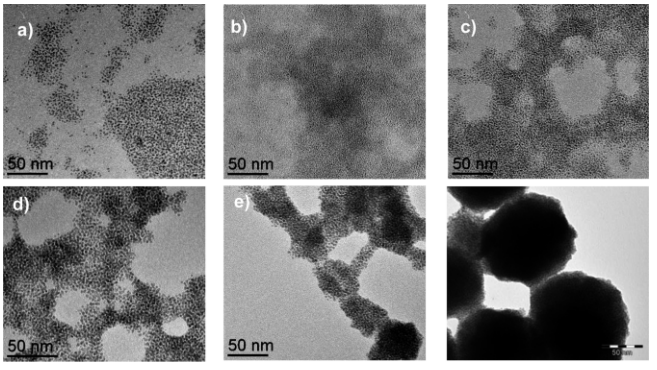

Figure 1. a) Ru@**TPhC** with a Ru/L ratio of 10:1; and **Ru@TPhTC** with Ru/L ratio of b) 4:1; c) 20:1; d) 40:1; e) 70:1 and f) **Ru@AdDC** with Ru/L ratio of 10:1.[15a] (Scale bar = 50 nm).

HRTEM and HAADF-STEM analyses were also performed on several samples (Figure 2) with different Ru/L ratio. Structural analysis performed on the HRTEM images of the rare NP found not aggregated, indicated that interplanar distances and angular relationships measured by 2D Fast Fourier Transform (2D-FFT) analysis are consistent with single Ru crystalline domains mostly showing the Ru hexagonal structure and quite seldom the Mn-β cubic one.[29] The evidence of this is provided by the HRTEM images displayed in Figure 2a, and it becomes apparent when observing the 2D-FFT patterns calculated on the Regions Of Interest (ROI) corresponding to distinct crystalline domains. One single crystal domain per particle can be clearly observed. In the case of Ru NP, at times the close proximity of single crystalline seeds could appear as a sort of an elongated particle composed by different crystalline domains (see the right-hand side of Figure 2a). However, both the presence of small discontinuities in these groups of close NP, and the different arrangements observed for the atomic columns in different parts of them, together with the different lattice spacing and zone axes detected, concur to indicate that the structures apparently ap-

Table 1. Mean size distributions, interparticle distances, ruthenium content, CO infrared frequency band of the Ru NP and Ru NP networks.

Catalyst	Ratio	Ru content [%][a]	NP size [nm][b]	NP size [nm][c]	Interparticle distance [nm][d]	ν_{CO} [cm^{-1}][e]
Ru@TPhC	10:1	–	1.7 ± 0.7	–	–	1928
Ru@TPhTC	4:1	14.4	1.3 ± 0.3	1.3–1.4	–	1935
Ru@TPhTC	20:1	50.6	1.3 ± 0.5	1.8	2.4	1939
Ru@TPhTC	40:1	66.0	1.7 ± 0.8	2.1	2.9	1935
Ru@TPhTC	70:1	66.1	1.9 ± 0.7	2.2	3.1	1926
Ru@HF	120:1	65.9	2.2 ± 1.8	2.3	3.0	1922

[a] By ICP. [b] By TEM. [c] By WAXS. [d] From SAXS. [e] By ATR-IR.

pearing as an elongated seed are just constituted by different NP in close vicinity. Some further consideration is deserved by the detection of a sole particle displaying Mn-β cubic structure (Figure 2a). It is known that the HRTEM could provide with local structural analysis of the particles it images, but, in case of concomitant presence of different crystal phases, such technique is not capable to quantitatively determine which among the phase is majority. This is due not only to the fact that HRTEM generally investigates the crystal structure of a very limited number of particles, but also that some phases may be less detectable than others. Indeed, this is the case of Ru NP with Mn-β cubic structure, of which the contrast is lower than the one of the NP showing their expected hexagonal structure. Such an effect combines with the NP very low size (about 1.5 nm), which further contributes to make their structure less clear. Thus, the HRTEM imaging is just indicating that the Ru NP contained in the sample with Ru/L ratio of 6:1 show both the hexagonal and the Mn-β cubic crystal structure.

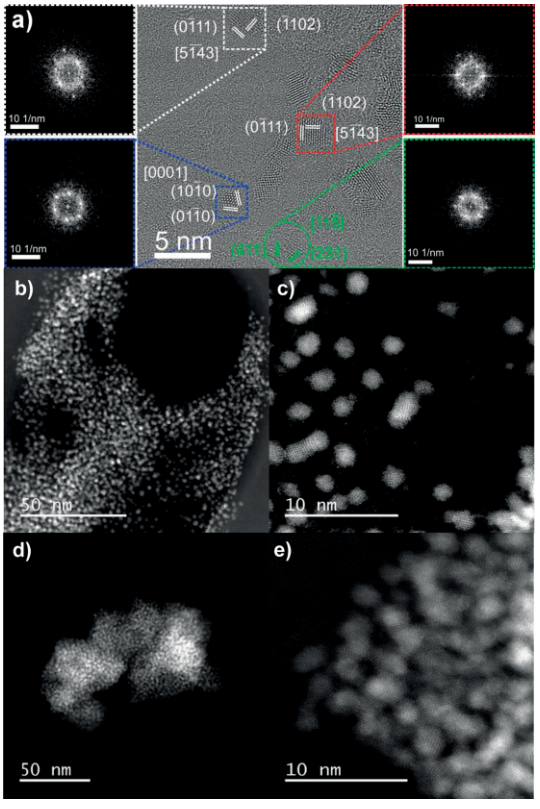

Figure 2. a) and b) HRTEM images of **Ru@TPhTC** with a Ru/L ratio of 6:1 - structural analysis was performed on the single crystalline seeds: the lattice spacings and zone axes are indicated in the HRTEM panels along with the ROIs used to calculate the 2D-FFT patterns (reported in both right and left panels). The Ru NP showing both the expected hexagonal and cubic Mn-β structure are enclosed by square- and round-shaped frames, respectively. b)-e) HAADF-STEM images of: b) and c) **Ru@TPhTC** with a Ru/L ratio of 20:1; and d) and e) **Ru@TPhTC** with a Ru/L ratio of 40:1.

At a Ru/L ratio of 20:1, small quantities of clusters and even Ru isolated atoms are shown around the NP in assemblies (Figure 2b and c). The Ru NP assemblies produced with a Ru/L ratio of 40:1 only display NP with Ru *hcp* crystalline structure excluding Ru single atoms (Figure 2d and e), in agreement with the WAXS analyses (Figure S4 of the SI). The WAXS analyses revealed well-crystallized Ru NP in the *hcp* structure for samples with a Ru/ligand ratio > 4. With the exception of **Ru@TPhTC** with a Ru/L ratio of 4:1, which shows a very distorted structure, all samples are consistent with metallic Ru NP in the *hcp* structure (Figure S4, top). This is confirmed in the RDF (Figure S4, bottom) where similar patterns are observed. From the coherence length, the size of the crystallites can be estimated to 2.2 nm for **Ru@TPhTC** - 70:1, 2.1 nm for **Ru@TPhTC** - 40:1, 1.9 nm for **Ru@TPhTC** - 20:1 and only 1.3 nm for **Ru@TPhTC** - 4:1. The **Ru@TPhTC** - 4:1 sample lacks characteristics from the *hcp* structure and can be described as crystallized in the metastable β-Mn structure,[29] as often observed for these very small sizes.[30] This is likely the effect of the high ligand/metal ratio that contributes to quench Ru NP growth right after the nucleation step.

Additionally, it is worth noting that the low contrast observed on the TEM micrographs would suggest that the assemblies obtained are relatively thin in comparison to the ones obtained with non-planar ligands such as polymantanes (both adamantane and diamantane) dicarboxylic (Figure S3g and h).[15a] This result suggests that the synthesis of 2D covalent assembly of Ru NP is possible via the use of ligands containing the planar triphenylene backbone. In order to corroborate the two-dimensional nature of these assemblies, further characterizations have been performed on these materials, including electron tomography and atomic force microscopy (AFM). AFM is commonly used to determine the thickness of 2D materials.[31] As shown in Figure 3a, the material **Ru@TPhTC** synthesized using a Ru/L ratio of 40:1 spreads evenly on the surface of the wafer. Due to the difference in height and substrate of the area covered by the material, the morphology and height information of the sample can be clearly observed. The objects have a measured thickness ranging from 3 to 12 nm (Figure 3b, c and Figure S5 of the SI). Considering that the size of the Ru NP is around 2 nm and taking into account the size of the ligand estimated from small angle X-ray scattering (SAXS) analyses (approximately 1 nm, see below), the thickness of the assembly corresponds to one to four layers of metal NP. Besides, the lateral size of the objects ranges from 0.1 to 1 μm, presenting a high aspect ratio, thereby confirming their 2D layered structure.

The 3D reconstruction obtained via electron tomography (see Figure 3e) confirms that the sample **Ru@TPhTC** – 40:1 is constituted by small NP with spherical shape. Besides, the 3D reconstruction of a large NP assembly (see Figure S6) allowed to study the interparticle distance for different positions and heights in the same quite large assembly of them. With this aim, the NP mutual distances in the assembly have been sampled in three diverse positions on the x-y plane, and at three diverse height from the bottom, which is basically represented by the TEM carbon grid where the particles were deposited. The three histograms reported in Figure S6 clearly show that the interparticle distance in different parts (i.e., volumes corresponding to the three colored boxes) of the large NP assembly is about the same, and equal to a mean value of 2.4 ± 1.2 nm.

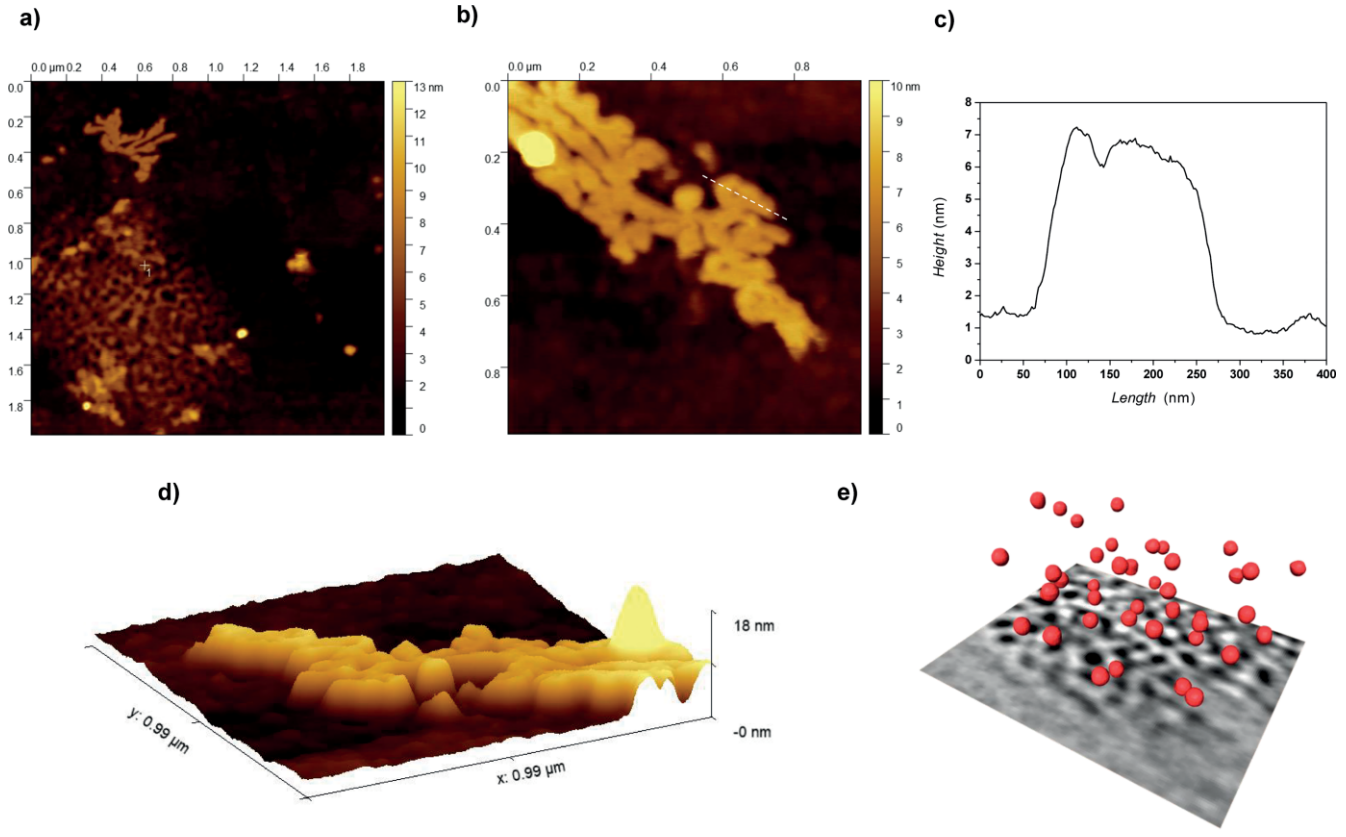

Figure 3. a) and b) AFM height images of **Ru@TPhTC** using 40:1 Ru/L ratio with c) height profile along the white dotted line; d) 3D rendering of the assembly; and e) 3D reconstruction of **Ru@TPhTC** – 40:1 via electron tomography, where just some particles are imaged to provide a direct evidence of their spherical shape.

SAXS analyses were also performed to reveal the arrangement of Ru NP inside the assembly and the appearance of the assembly of NP. A Kratky plot ($q^2I(q)$ vs. q) was employed to highlight the different broad peaks of the X-ray scattering curves (Figure 4). The SAXS data can be described as the scattering from a multiscale organization of Ru NP assembly with a sum of three contributions:

I(q)global = I(q)surface + I(q)corr + I(q)sphere * S(q)

To describe the region at low angles, we use a first term $I(q)_{surface}$ that follows a power law function. The value of the exponent reflects the roughness of the surface of the NP assembly. All SAXS curves present at intermediate angles (0.01–0.03Å^{-1}) a broad peak reflecting the presence of a correlation distance and can be described by the second term $I(q)_{corr}$ based on adjustable Lorentzian function. The high angles contain structural information on elementary Ru NP such as NP mean diameter and mean interparticle distance, and can be modelled with an equation of sphere $I(q)_{sphere}$ multiplied by a structural factor $S(q)$. All data were fitted with the model described above and the adjustable parameters are summarized in Table S1. The first parameter corresponding to exponent of power law function (P) is close to 4 for **Ru@TPhTC** 20:1 (4) and **Ru@TPhTC** 70:1 (3.8) samples, corresponding to a well-define and smooth interface. For **Ru@TPhTC** 40:1, this value decreases at 3.2 corresponding to a rougher surface such as for the surface of fractal objects.[32] The correlation length observed at intermediates angles (ξ = 5–11 nm) could correspond to the thickness of the

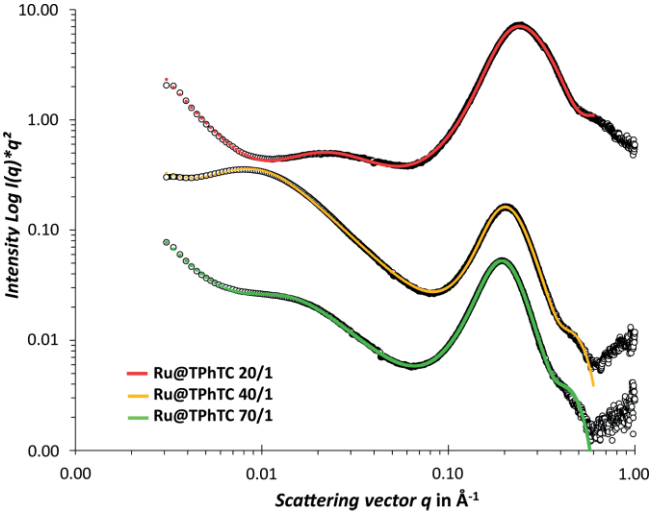

Figure 4. SAXS patterns of Ru NP assemblies produced with the **TPhTC** ligand (red curve, **Ru@TPhTC** - 20:1, yellow curve, **Ru@TPhTC** - 40:1, and green curve, **Ru@TPhTC** - 70:1). The experimental SAXS curves are plotted in log $I(q)q^2$ *fct* log q representation in black line and the fitting curves corresponding to the calculated SAXS curves from the model are plotted in dashed line.

layers. The measured values are consistent with those obtained by AFM. The radius of the elementary Ru NP (R) increases slightly with the proportion of ligand, giving a sphere radius comprised between 0.75 and 1.2 nm consistent with EM obser-

vations (0.65–0.95 nm). The peaks at high angle (> 0.1Å^{-1}) represent the average distance between NP detected at 0.18, 0.20 and 0.22 Å^{-1} for **Ru@TPhTC** samples 70:1, 40:1 and 20:1. The correlation distances were calculated displaying the average of interparticle distances (R_{eff}) at 3.1, 2.9 and 2.4 nm, for samples 70:1, 40:1 and 20:1, respectively. As the length of the ligand is the same for all Ru NP series this variation on the distance is caused by the different Ru NP mean size diameter (1.9 ± 0.7, 1.7 ± 0.8, and 1.3 ± 0.5 nm, for **Ru@TPhTC** - 70:1, 40:1 and 20:1, respectively), which fits well with a distance of about 1 nm for all cases due to the presence of the ligand (Table 1). The mean interparticle distance determined by ET for **Ru@TPhTC** samples 40:1 (2.4 ± 1.2 nm) is in reasonable agreement with the SAXS analysis (2.9 nm).

Finally, the thermal stability of the **Ru@TPhTC** - 40:1 was evaluated by TPD/MS (Figure S7). Decarboxylation occurs at 190 °C, as ascertained by the detection of CO_2. As the temperature increases, decarbonylation (CO desorption) and decarboxylation (CO_2 desorption) is detected at around 300–400 °C. As comparison, the **TPhTC** ligand decomposed in the temperature range of 420–440 °C, which indicates the decomposition is facilitated by Ru NP.

2.2 Synthesis and Characterization of 3D Ru NP Assemblies

Likewise, Ru NP assembled with the **HF** ligand were synthesized straightforwardly from [Ru(η^4-C_8H_{12})(η^6-C_8H_{10})] under 3 bar of H_2 at room temperature using a Ru/ligand ratio of 120:1, which corresponds to a Ru/functional group ratio of 10:1. The **HF** ligand was prepared for the first time in this work, and its synthesis consists in a two-step procedure. First, a malonate derivative containing two alkyne groups reacts through a Bingel-Hirsch reaction with the fullerene C_{60}, followed by an alkyne-azide 1,3-dipolar cycloaddition to give **HF** compound in low yield (see details in experimental section). The formation of a 3D assembly of Ru NP was first confirmed by TEM analyses (Figure 5a); the size of the NP is 2.2 ± 1.8 nm. WAXS analyses confirmed that the Ru NP are well-crystallised in the *hcp* structure with a mean particle size of 2.3 nm (Figure S8). SAXS analyses of the **Ru@HF** sample (Figure 5b) revealed an interparticle distance of 3.0 nm.

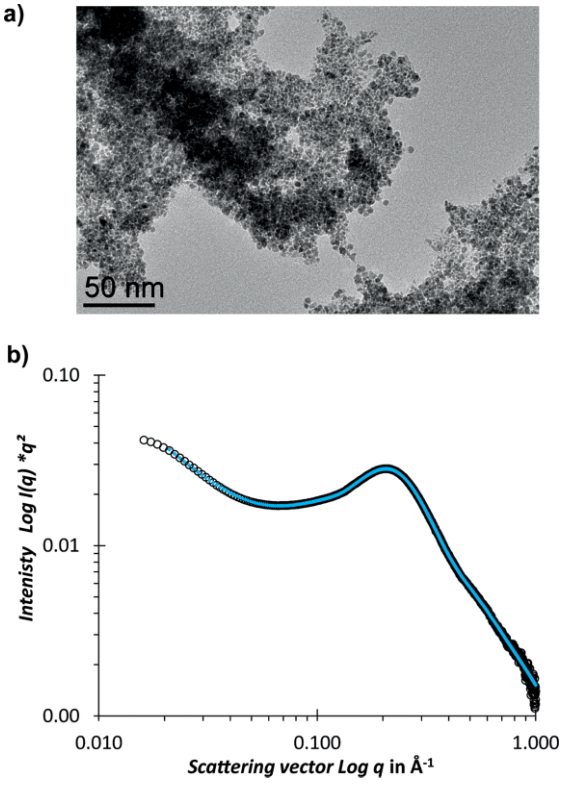

Figure 5. a) TEM image and b) SAXS pattern of **Ru@HF** produced using a Ru/ligand ratio of 120:1.

In that case, the peak is very broad, which was attributted to the broad Ru particle size distribution (Figure S3f). Comparing to the Ru NP assemblies described in a previous work by using the hexa-substituted fullerene C_{60}, **Ru@C_{66}(COOH)$_{12}$** linker,[15b] the interparticle size is larger with **HF**, since the interparticle distance for **Ru@C_{66}(COOH)$_{12}$** was 2.8 nm, with a Ru NP size of 1.5 ± 0.8 nm. Thus and as expected, the presence of the intermediary long chains present in **HF** allows increasing the interparticle distance.

2.3 Surface Coordination Chemistry

The coordination of the stabilizing ligand onto the Ru NP surface has been investigated by means of spectroscopic techniques, including IR, solid state NMR using magic angle spinning (MAS NMR), and X-ray photoelectron spectroscopy (XPS). It has been previously demonstrated by some of us[15a,15b,33] and others,[34] that carboxylic acid groups coordinate to the Ru NP surface after losing their proton, giving rise to carboxylate species together with surface hydrides. The carboxylate surface species can be easily detected using IR spectroscopy; thus, the IR spectra of the **Ru@TPhTC** samples produced at different Ru/ligand ratio have been recorded and analyzed (Figure 6a). The characteristic peak due to the C=O stretching of the carboxylic acid groups of the ligand at 1680 cm^{-1} (Figure 6a, bottom), vanishes in **Ru@TPhTC** samples, generating a new set of peaks appearing at around 1578 and 1376 cm^{-1}, assigned, respectively, to the antisymmetric ($\nu_{as}(COO^-)$) and symmetric ($\nu_s(COO^-)$) stretching vibrations of the carboxylate group. The difference between $\nu_{as}(COO^-)$ and $\nu_s(COO^-)$ ($\Delta\nu$) in the IR spectra is generally used to determine the coordination mode of the carboxylate group.[35] For **Ru@TPhTC** samples, a $\Delta\nu$ of about 202 cm^{-1} was measured, which is attributed to a bridging bidentate mode; in line with our previous results.[15a] Other characteristic peaks of the ligand, such as the intense peaks at 1251 and 1164 cm^{-1} corresponding to the ether bonds, or the peaks assigned to the triphenylene aromatic backbone, which appear in the range of 1500–1600 cm^{-1}, are observed in all spectra, pointing out that the ligand is stable under the synthetic conditions. An intense band at 1932 cm^{-1} was also observed in all Ru samples, which indicates adsorbed CO on the Ru NP surface; probably resulting from the decarbonylation of the carboxylic acid and decomposition of the solvent of the reaction, THF, as experimentally and theoretically demonstrated elsewhere.[15a] In the case of the sample **Ru@TPhTC** with Ru/L

ratio of 70:1, the intensity of this band is weak, presumably because of a prolonged outgassing of this sample before analysis, which favors CO desorption.[15a]

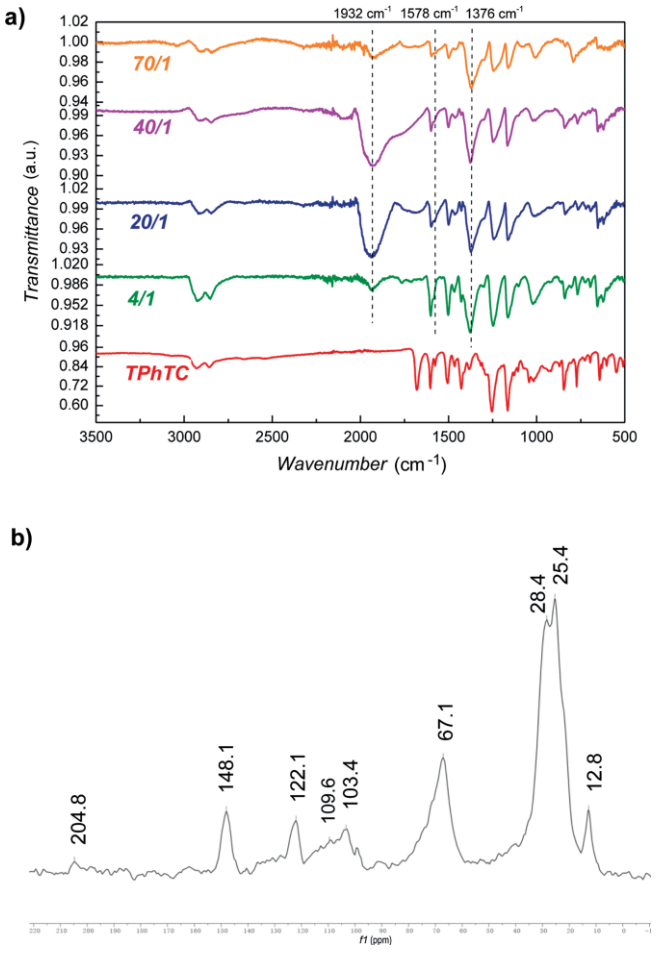

Figure 6. a) ATR-IR spectra of **TPhTC** and **Ru@TPhTC** with Ru/L ratio from 4:1 to 70:1 (from bottom to top); and b) ^{1}H-^{13}C CP MAS SS-NMR spectrum of **Ru@TPhTC** with a Ru/L ratio of 40:1.

MAS NMR with and without ^{1}H-^{13}C cross polarization (CP) were recorded for **Ru@TPhTC** - 40:1 sample, and the ^{1}H-^{13}C CP MAS SS-NMR spectrum is depicted in Figure 6b (^{13}C NMR of the free ligand is shown on Figure S9). Peaks at 12.8, 25.4, 28.4 ppm are attributed to the carbons of the alkyl chain, which link the triphenylene core to the carboxylic acid moieties. The broad peak centered at 67.1 ppm corresponds to the saturated carbons of the ether bonds besides the aromatic ring. The aromatic carbons appear in the range of 103.4 to 148.1 ppm. Although hydrogenation of triphenylene with Ru NP have been reported at 30–80 °C and 20 bar H_2,[36] we did not find traces of hydrogenation of the triphenylene core under our conditions.

XPS of **Ru@TPhTC** - 40:1 (Figure S10, Table S2) reveals the presence of metallic Ru through the presence of two doublet peaks of Ru *3d* at 279.9 and 284.1 eV, and Ru *3p* at 461.5 and 483.7 eV.[37] The C *1s* peak was deconvoluted into three contributions at 285.0 (C-C and C-H bonds), 286.4 (C-O bonds from ether bonds), and 288.1 eV (O=C-O bonds). Two peaks at 530.8 and 532.3 eV of O *1s* are in agreement with a carbonyl group and a weak peak at 529.5 eV with a Ru–O bond, suggesting that the Ru is coordinated to the ligand through oxygen atoms as observed before for Ru-carboxylate nanostructures.[15b]

Concerning **Ru@HF**, infrared analysis show that, upon coordination of the **HF** ligand on the Ru NP surface, two new bands appear at 1580 and 1395 cm^{-1}, (Figure S11a) together with the disappearance of the signals at 1720 cm^{-1} (C=O stretching), when compared to the free **HF** ligand, corresponding to carboxylate species coordinating to the Ru surface through a bridging bidentate mode ($\Delta\nu$ = 185 cm^{-1}). Adsorbed CO species were also detected with a band at 1922 cm^{-1}. The other bands due to the ligand remained unchanged, which was attributed to the stability of the ligand under synthetic conditions. The triazole unit is identified by a band at 1551 cm^{-1} due to the N=N bond,[38] and 1440 cm^{-1} due to N-C stretching.[39] The band at 1731 cm^{-1} is due to the six carboxylate groups of the malonate cycloadduct. The ^{13}C SS-NMR spectrum (Figure S11b) shows the presence of the ligand in the heterostructure. Characteristic peaks of the 1,2,3- triazole unit (120.1 and 63.4 ppm), the fullerene cage (141.4 and 66.2 ppm), quaternary carbon of the cyclopropane (50.0 ppm) and the carbon atoms of the alkyl chains (25.2 ppm) were detected in the spectrum.

These characterizations point for a similar stabilization of the Ru NP in the 2D and 3D assemblies, which involves the coordination of the **TPhTC** and **HF** ligands through the carboxylate bridging bidentate mode.

2.4 Hydrogenation of Phenylacetylene

Semi hydrogenation of phenylacetylene is an useful process to purify styrene produced for polymerization.[40] From an environmental point of view and cost, it has been shown that ruthenium is a greener heterogeneous catalyst compared to other noble metals.[41] Surprisingly, even if colloidal Ru NP are usually highly efficient (selective) hydrogenation catalysts,[42] reports on the application of Ru NP for this specific catalytic reduction are relatively scarce.[16a,43] We recently evidenced that for 3D Ru NP assemblies produced from polymantane ligands, the Ru NP interparticle distance (steric effect) and electronic effects control the catalyst activity and selectivity.[15a] Increase of activity was evidenced for electron rich Ru NP and/or for short interparticle distances. Oppositely, an increase of selectivity towards styrene was observed on electro-deficient Ru NP and/or for long interparticle distances.

In this context, the 2D and 3D assemblies here prepared were used as catalysts in the semi-hydrogenation of phenylacetylene to styrene under mild conditions, i.e. room temperature and a constant H_2 pressure of 5 bar. The results are listed in Table 2. Time-conversion/selectivity curves are presented on Figure 7.

We analyzed the results obtained here in terms of steric and electronic effects, which are correlated to interparticle distance and ν_{CO} of the CO adsorbed onto the Ru NP surface, respectively. The ν_{CO} frequency, which is a probe for the electronic effect of the ligands onto the Ru NP surface,[42] is different for the two samples, being (in cm^{-1}): 1922 (**Ru@HF**) and 1935 (**Ru@TPhTC**); indicating a higher electronic density on the Ru NP in the **Ru@HF** sample. When the electron density at the NP

Table 2. Hydrogenation of phenylacetylene using Ru catalyst.[a]

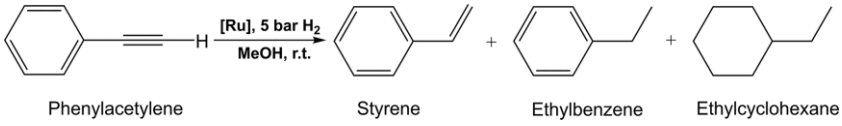

Entry	Catalyst	Time [h]	Conv. [%]	$S_{20\,\%}$ [%]	$S_{60\,\%}$ [%]	TOF [h^{-1}][b]	TOF_s [h^{-1}][c]
1	**Ru@TPhTC** - 40:1	5	64.0	57.5	53.5	46.5	15.6
2	**Ru@HF** - 120:1	3	86.1	59.5	51.2	134.3	70.2
3	**1.6 %Ru/O-CNT**[15a]	8	10.6	67.8[d]	–	3.8	5.8[e]

[a] Reaction conditions: 0.02 mmol of Ru, 412 mg (4.00 mmol) of phenylacetylene, 71 mg (0.50 mmol) of decane (internal standard), room temperature, 5 bar H_2, 25 mL of MeOH. [b] TOF in $mol_{PAconverted}\ mol_{Ru}^{-1}\ h^{-1}$ calculated according to surface Ru content at the time given in column reporting the reaction time. [c] TOF calculated according to surface Ru content at 1 h. [d] Selectivity calculated at 10 % conversion. [e] TOF calculated according to surface Ru content at 8 h and Ru dispersion calculated as described in ref.[44].

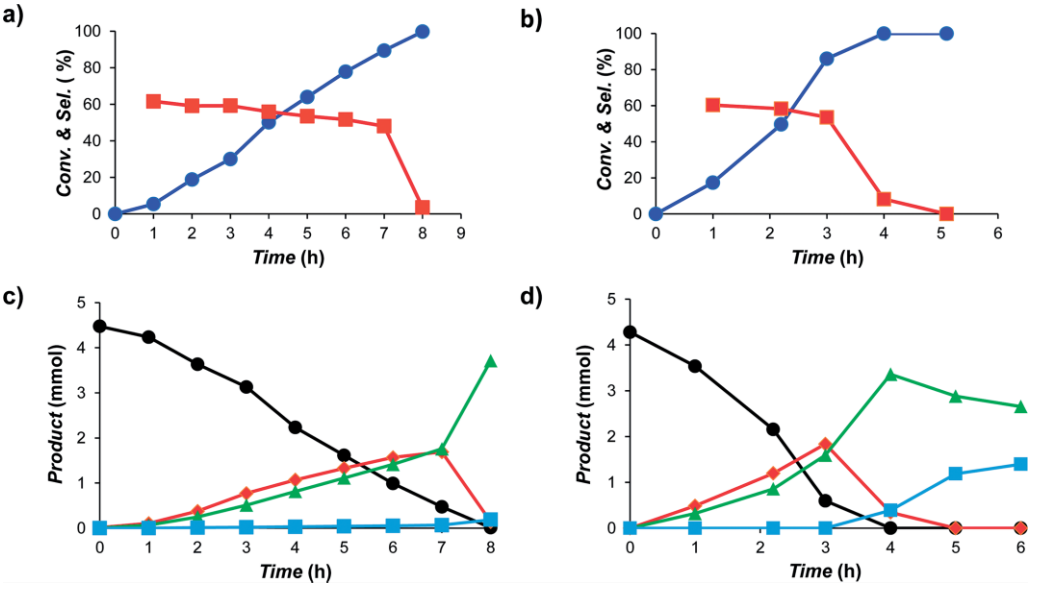

Figure 7. Evolution of conversion (blue lines) and selectivity toward styrene (red lines) over time for the investigated catalysts: a) **Ru@TPhTC** - 40:1 and b) **Ru@HF** - 120:1; product distribution over time for: c) **Ru@TPhTC** - 40:1; and d) **Ru@HF** - 120:1. (Black circle phenylacetylene, red diamond styrene, green triangle ethylbenzene, and blue square ethylcyclohexane).

surface increases, favoring thus the π back-donation from the *d* Ru orbitals to the antibonding π* orbital of the alkyne/alkene, we can expect a facilitated hydrogenation. Conversely, if the charge transfer from the metal to the ligand results in electrodeficient Ru NP providing less π back-donation to the alkene, a weakened Ru–alkene bonding is obtained, which favors its quick desorption, and avoids overhydrogenation to produce ethylbenzene. From the results obtained we could thus expected that the **Ru@HF** catalyst will be more active, but less selective than **Ru@TPhTC**.

Both catalysts were active for this hydrogenation reaction displaying turnover frequencies (TOF) of 46.5 h^{-1} for **Ru@TPhTC** and 134.3 h^{-1} for **Ru@HF**. The selectivity towards styrene is similar for both catalysts and relatively high (50–60 %) and constant over time, up to 90 % conversion. In this conversion range, the main products of reaction are styrene and ethyl benzene for both catalysts. Above 90 % conversion the selectivity abruptly decreases due to the formation of ethylbenzene and then ethylcyclohexane (Figure 7). The total hydrogenation of phenylacetylene under relatively mild reaction conditions using supported[43a] or colloidal[43c] Ru NP as catalysts has already been reported and is not surprising, even at room temperature. **Ru@HF** - 120:1 displayed the highest activity, which correlated well with the fact that the Ru NP in **Ru@HF** display the highest electron density. The fact that both catalysts present a similar selectivity cannot be correlated to this electronic effect.

As far as steric effects are concerned, it is thus worth noting that from SAXS data these two catalysts present a similar interparticle distance. However, we can postulate that considering the molecular structure of the **HF** ligand (Scheme 2) a more sterically crowded environment should exist around the Ru NP in the 3D **Ru@HF** architecture than in the 2D **Ru@TPhTC** one. If this is the case, the higher TOF obtained with **Ru@HF** would be in phase with a CE, as previously reported.[15a] However, there also the selectivity towards styrene should be lower for the **Ru@HF** catalyst in comparison with **Ru@TPhTC**.

A general tendency generally observed for ligand protected NP catalysis is that the cleaner the metal surface, the higher

the activity and the lower the selectivity.[45] In this sense, if we consider the Ru/L molar ratio calculated from elemental and ICP analyses, it is around 73 and 22.5 for the **Ru@HF** and **Ru@TPhTC** catalysts, respectively. If we take into account the Ru NP size, this roughly corresponds to -COOH/Ru_{surf} ratio of 0.35 and 0.23 for the **Ru@HF** and **Ru@TPhTC** catalysts, respectively (see experimental section for calculations). The lower ratio obtained with the **TPhTC** ligand (cleaner metal surface) should contribute to an increased activity and a decreased the selectivity, which is not the observed tendency. Thus, as none of the classical ligand effects observed in selective hydrogenation can satisfactorily explain the performances obtained in terms of both activity and selectivity, we tentatively attributed the specific behavior of the **Ru@TPhTC** catalyst (lower activity and similar selectivity than **Ru@HF**) to the different spatial ordering of the sample, 2D, in contrast to the 3D networks displayed for **Ru@HF**. In the 2D assembly, the ratio between confined/unconfined Ru NP should be much smaller than for the 3D assemblies. These less marked effects of confinement, combined with the electronic effects brought about by the ligands must be at the origin of the lower performances obtained with the **Ru@TPhTC** catalyst.

To better delineate the performances of the Ru NP networks prepared from the functionalized ligands we compared their reactivity with the ones of individual unprotected Ru NP deposited on carbon nanotubes functionalized with nitric acid (O-CNT)[15a] that contains significant amounts of carboxylic groups to stabilize Ru NP.[33] This catalyst present Ru NP size of 1.5 nm (Figure S12) and show much lower conversions (Table 2, entry 3 and Figure S13) than the Ru NP networks. For this catalyst, in which the Ru NP are not confined, the selectivity towards styrene is higher than for the 2D and 3D NP networks. At low conversions (< 10 %) the two products of the reaction are styrene and ethyl benzene. High selectivity towards styrene and relatively low activity are often obtained on supported or colloidal Ru NP (see Table S3 for representative examples from the literature). It thus appears that the confined Ru NP networks prepared in this work present a lower selectivity than many catalytic systems based on supported or colloidal Ru NP. CE have been regularly reported to have a beneficial impact on catalyst selectivity towards styrene in phenylacetylene hydrogenation, the CE facilitating desorption of styrene from metallic NP surface.[46] However, it is important to note that in our confined catalysts the metal loading is extremely high (> 60 % w/w). Thus, the Ru NP density is extremely high and the probability that a desorbed styrene molecule reached a new Ru NP to be further hydrogenated is much higher than in the case of conventional confined catalysts (see Scheme 1).

The different catalysts prepared from **TPhTC** and **HF** linkers were also analyzed by ICP and TEM after the catalytic reaction (Figure S14 and Table S4). In all cases, the NP after catalysis are slightly more aggregated, making the determination of their size distribution more difficult. Surprisingly, the average NP sizes is smaller than before the catalytic test. As this could be the result from metal leaching, the ruthenium leaching was determined by ICP analyses of the liquid phase after catalysis. Assemblies of **TPhTC** did not show any leaching, while for **HF** ligand it was determined to be only 0.25 %. We therefore attribute this surprising result to the precision of the TEM measures since after catalysis the NP are more aggregated, which is not the case before catalysis. It is also worth mentioning that we cannot discard a possible redispersion of the metallic phase after catalysis with the formation of Ru single atoms. Although we have not performed STEM-HAADF analyses to confirm that possibility, this phenomenon has already been reported for Ru/C catalysts.[47]

These results highlight the good stability of the covalent assemblies prepared as already reported in our previous studies.[15a]

3. Conclusion

We have demonstrated here that the careful choice of the ligand allows producing in a controlled manner assemblies of Ru metallic NP, which can be ordered in 2D or 3D networks. The networks of small Ru NP are synthesized straightforwardly under mild synthetic conditions. We have shown that electronic and steric effects can be finely tuned, and therefore the catalytic properties of the materials. It has already been shown that long interparticle distances can be detrimental for activity in the selective hydrogenation of phenylacetylene (weak CE), while electron-deficient Ru surfaces can provide higher selectivity towards the semi-hydrogenated product.[15a] The present work proves that this is not always the case and that the dimensionality of the NP networks should also be considered. Even if instinctively 2D networks of metal NP should provide more active catalysts, as *a priori* metal surface should be more readily available, here it is not the case, argument which gives strength to the importance of confinement effects, which seem to be more easily reached when using 3D networks of metal NP.

4. Experimental Section

4.1 General Methods: Solvents were purified by standard methods or by an MBraun SPS-800 solvent purification system. 4-pentyn-1-ol, triethylamine, 4-dimethylaminopyridine, malonyl chloride, CBr_4, C_{60} fullerene, 1,8-diazabicyclo[5.4.0]undec-7-ene (DBU), sodium azide (NaN_3), 6-bromohexanoic acid, KI, CuBr•SMe_2, sodium ascorbate, QuadraSil® MP, phenylacetylene and decane were purchased from Sigma-Aldrich and used as received. [Ru(COD)(COT)] [(1,5-cyclooctadiene)(1,3,5-cyclooctatriene)ruthenium] was purchased from Nanomeps Toulouse, CO and H_2 from Air Liquid. For column chromatography silica gel 60 (230–400 mesh, 0.040–0.063 mm) was purchased from E. Merck or by Sephadex LH20 (GE Healthcare, Barcelona, Spain) gel filtration.

Microwave irradiation experiments were performed using a Monowave 300 (Anton Pear) apparatus. The temperature in the sealed reaction vessel was monitored by an external surface sensor.

4.2 Characterization: The details of characterizations techniques used in this work are provided in the Method section in the SI).

4.3 Ligand Synthesis

Synthesis of Carboxylic Functionalized Triphenylene (TPhC)

2-(4-(Methoxycarbonyl)phenoxy)hexyloxy)-3,6,7,10,11-pentakis-(hexyloxy)triphenylene (1): (Scheme 3) A mixture of 3,6,7,10,11-

pentakis(hexyloxy)triphenylen-2-ol[48] (1.22 g, 1.64 mmol), methyl-4-(6-bromohexyloxy)benzoate[48] (1.80 g, 5.73 mmol), and anhydrous K_2CO_3 (0.80 g, 1.44 mmol) in 100 mL of dry butanone was refluxed under nitrogen atmosphere for 24 h. After cooling to room temperature, the solvent was removed under vacuum, and then water (200 mL) was added. The mixture was extracted with dichloromethane (5 × 30 mL). The organic fractions were combined and dried with $MgSO_4$. Filtration followed by solvent removal afforded the crude product, which was purified by column chromatography (silica gel, dichloromethane/hexane 1:3 v/v). The compound was isolated as light yellow solid (1.33 g, 83 % yield). ^{1}H NMR ($CDCl_3$, 500 MHz) δ(ppm) = 7.97 (d, 2H, ArH, AA′ part of AA′XX′ spin system, $N = J_{AX} + J_{AX'} = 8.98$ Hz, $J_{AA'} \sim J_{XX'}$), 7.83 (s, 6H, TripH), 6.90 (d, 2H, ArH, XX′ part of AA′XX′ spin system, $N = J_{AX} + J_{AX'} = 8.98$ Hz, $J_{AA'} \sim J_{XX'}$), 4.23 (m, 12H, TriPh-O-CH_2), 4.04 (t, 2H, ArH-O-CH_2, $J = 6.40$ Hz), 3.88 (s, 3H, O-CH_3), 2.02–1.84 (m, 14H, CH_2), 1.71–1.56 (m, 14H, CH_2), 1.44–1.33 (m, 20H, CH_2), 0.93 (m, 15H, CH_3). IR (cm^{-1}): ν (C=O): 1722.

2(6-(4-(Carboxy)phenoxy)hexyloxy)-3,6,7,10,11-pentakis(hexyloxy)triphenylene (TPhC): To a suspension of compound (**1**) (1.33 g, 1.36 mmol) in 140 mL of absolute ethanol, NaOH (1.69 g, 42.25 mmol) was added. After refluxing for 5 h, the solvent was removed on a rotary evaporator. Water (120 mL) and dichloromethane (50 mL) were added to the solid residue obtained, and the stirred mixture was treated with 36 % hydrochloric acid until pH = 2. The organic phase was collected and the water solution extracted again with dichloromethane (4 × 50 mL). The dichloromethane extracts were dried with anhydrous magnesium sulfate and filtered. The solvent was removed on a rotary evaporator to obtain the product as a light yellow solid, which was dried under

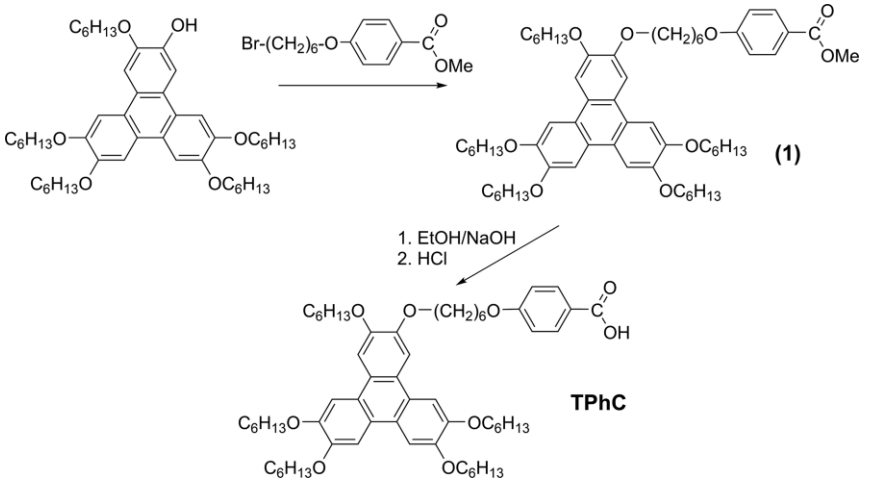

Scheme 3. Synthesis procedure of **TPhC**.

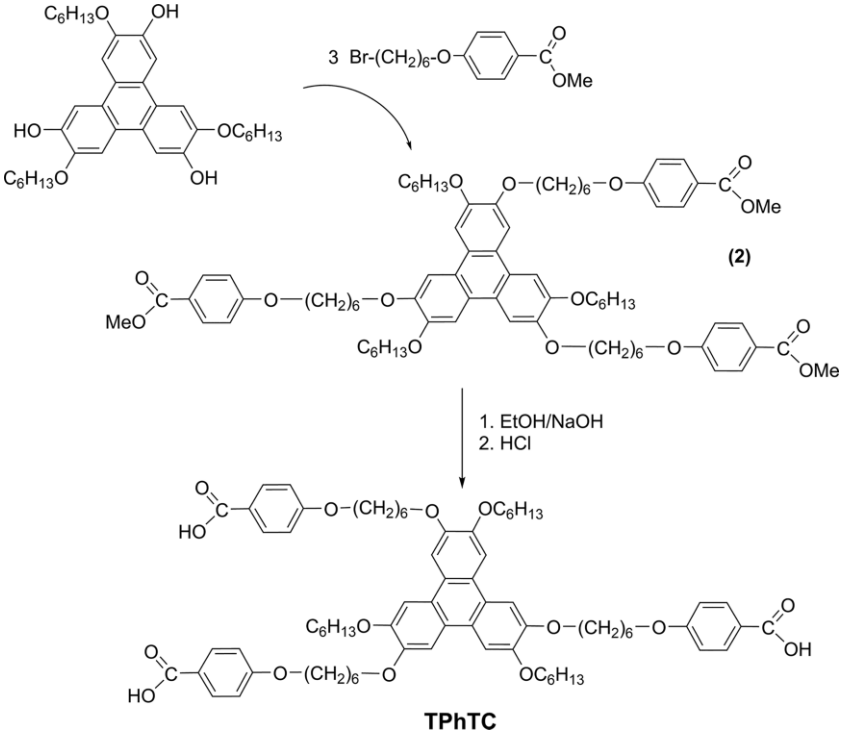

Scheme 4. Synthesis procedure of **TPhTC**.

vacuum. (1.21 g, 93 % yield). ^{1}H NMR ($CDCl_3$, 500 MHz) δ (ppm) = 10.86 (s, 1H, OH), 8.04 (d, 2H, ArH, AA′ part of AA′XX′ spin system, $N = J_{AX} + J_{AX'}$ = 9.01 Hz, $J_{AA'} \sim J_{XX'}$), 7.84 (s, 6H, TriPh), 6.93 (d, 2H, ArH, XX′ part of AA′XX′ spin system, $N = J_{AX} + J_{AX'}$ = 9.01 Hz, $J_{AA'} \sim J_{XX'}$), 4.23 (m, 12H, TriPh-O-CH_2), 4.06 (t, 2H, ArH-O-CH_2, J = 6.48 Hz), 2.02–1.86 (m, 14H, CH_2), 1.72–1.54 (m, 14H, CH_2), 1.45–1.34 (m, 20H, CH_2), 0.93 (m, 15H, CH_3). ^{13}C {^{1}H} NMR ($CDCl_3$, 126 MHz, Me_4Si) δ(ppm) = 171.43 (*C*=O), 163.60 (sp^2-C, O-C_{Ph}), 149.03, 149.02, 148.99, 148.97, 148.96, 148.85 (sp^2-C, O-C_{TriPh}), 132.32 (sp^2-C, H_A-C_{Ph}), 123.71, 123.67, 123.65, 123.58 (sp^2-C, C_{TriPh}), 121.41 (sp^2-C, HOOC-C_{Ph}), 114.16 (sp^2-C, H_x-C_{Ph}), 107.47, 107.46, 107.39, 107.36, 107.25 (sp^2-C, H-C_{TriPh}), 69.79, 69.74, 69.71, 69.62, 69.52, 68.10 (O-*C*H_2), 31.69, 31.67, 29.44, 29.43, 29.11, 25.98, 25.85, 22.66 (*C*H_2), 14.05 (*C*H_3). IR (cm^{-1}): ν (C=O): 1690. Anal. calcd. (%) for $C_{61}H_{88}O_9$: C, 75.90; H, 9.19; O, 14.92; found C, 75.78; H, 9.02. DSC (Transition temperature and enthalpy in parentheses; data referred to the second heating scan) = Crystal → Isotropic liquid 63.6 °C (33.2 kJ mol^{-1}).

Synthesis of Tricarboxylic Functionalized Triphenylene (TPhTC)

2,6,10-Tris(6-(4-(methoxycarbonyl)phenoxy)hexyloxy)-3,7,11-trihexyloxytriphenylene (2): (Scheme 4). A mixture of 2,6,10-trihydroxy-3,7,11-trihexyloxytriphenylene[49] (1.83 g, 3.17 mmol), methyl-4-(6-bromohexyloxy)benzoate[50] (9.00 g, 28.6 mmol), and anhydrous K_2CO_3 (15.79 g, 114.2 mmol) in 100 mL of dry butanone was refluxed under nitrogen atmosphere for 24 h. After cooling to room temperature, the solvent was removed under vacuum, and then water (100 mL) was added. The mixture was extracted with dichloromethane (3 × 30 mL). The organic fractions were combined and dried with $MgSO_4$. Filtration followed by solvent removal afforded the crude product, which was purified by column chromatography (silica gel, ethyl acetate/hexane 3:1 v/v). The compound was isolated as a light yellow solid (2.25 g, 55.4 % yield). ^{1}H NMR ($CDCl_3$, 500 MHz) δ (ppm) = 7.97 (d, 6H, ArH, AA′ part of AA′XX′ spin system, $N = J_{AX} + J_{AX'}$ = 8.92 Hz, $J_{AA'} \sim J_{XX'}$), 7.84 (s, 3H, TriPh), 7.83 (s, 3H, TriPh), 6.90 (d, 6H, ArH, XX′ part of AA′XX′ spin system, $N = J_{AX} + J_{AX'}$ = 8.92 Hz, $J_{AA'} \sim J_{XX'}$), 4.23 (m, 12H, TriPh-O-CH_2), 4.04 (t, 6H, ArH-O-CH_2, J = 6.40 Hz), 3.88 (s, 9H, O-CH_3), 2.02–1.84 (m, 18H, CH_2), 1.72–1.53 (m, 18H, CH_2), 1.38 (m, 12H, CH_2), 0.92 (t, 9H, CH_2, J = 6.92 Hz). IR (cm^{-1}): ν (C=O): 1716.

2,6,10-Tris(6-(4-(carboxy)phenoxy)hexyloxy)-3,7,11-trihexyloxytriphenylene (TPhTC): To a solution of 2,6,10-tris(6-(4-(methoxycarbonyl)phenoxy)hexyloxy)-3,7,11-trihexyloxytriphenylene[49] (1.90 g, 1.48 mmol) in 100 mL of absolute ethanol, NaOH (3.56 g, 89.1 mmol) was added. After refluxing for 6 h, the solvent was removed on a rotary evaporator. Glacial acetic acid (125 mL) was added and the mixture refluxed for 2 h giving rise to a white solid. The solid was collected by filtration, washed first with cold water (3 × 50 mL), then with cold acetone (3 × 50 mL) and finally dried under vacuum. (1.60 g, 87.1 % yield). ^{1}H NMR ([D$_6$]DMSO, 500 MHz) δ(ppm)= 12.56 (s, 3H, OH), 7.94 (s, 3H, TriPh), 7.93 (s, 3H, TriPh), 7.85 (d, 6H, ArH, AA′ part of AA′XX′ spin system, $N = J_{AX} + J_{AX'}$ = 8.92 Hz, $J_{AA'} \sim J_{XX'}$), 6.96 (d, 6H, ArH, XX′ part of AA′XX′ spin system, $N = J_{AX} + J_{AX'}$ = 8.92 Hz, $J_{AA'} \sim J_{XX'}$), 4.19 (m, 12H, TriPh-O-CH_2), 4.01 (t, 6H, ArH-O-CH_2, J = 6.42 Hz), 1.85–1.71 (m, 18H, CH_2), 1.63–1.42 (m, 18H, CH_2), 1.35–1.22z (m, 12H, CH_2), 0.82 (t, 9H, CH_3, J = 6.87 Hz). ^{13}C {^{1}H} NMR ([D$_6$]DMSO, 126 MHz, Me_4Si) δ(ppm) = 167.44 (*C*=O), 162.72 (sp^2-C, O-C_{Ph}), 149.00, 148.98 (sp^2-C, O-C_{TriPh}), 131.75 (sp^2-C, H_A-C_{Ph}), 123.39, 123.35 (sp^2-C, C_{TriPh}), 123.26 (sp^2-C, HOOC-C_{Ph}), 114.56 (sp^2-C, H_x-C_{Ph}), 107.55, 107.49 (sp^2-C, H-C_{TriPh}), 69.13, 69.08, 68.12 (O-*C*H_2), 31.53, 29.35, 29.05, 25.97, 25.83, 25.76, 22.58 (*C*H_2), 14.29 (*C*H_3). IR (cm^{-1}): ν (C=O): 1678. Anal. calcd. (%) for $C_{75}H_{96}O_{15}$: C, 72.79; H, 7.82; found C, 72.81; H, 7.70. DSC (Transition temperatures and enthalpies in parentheses; data referred to the second heating scan) = Glass → Nematic 58.5 °C, Nematic → Isotropic liquid 113.6 °C (3.3 kJ mol^{-1}).

Synthesis of Hexa-Substituted Fullerene (HF)

Di(pent-4-yn-1-yl) Malonate (1): (Scheme 5) 4-pentyn-1-ol (0.88 ml, 9.46 mmol), NEt_3 (1.34 mL) and 4-dimethylaminopyridine (DMAP) (11.56 mg, 0.0946 mmol) were successively dissolved in dichloromethane (25 ml) under inert atmosphere. The mixture was cooled down to 0 °C, and a solution of malonyl chloride (0.47 mL, 4.73 mmol) in 1–2 mL of dichloromethane was added dropwise. After 30 min, the reaction mixture was warmed up to room temperature and stirred overnight. The reaction solution was treated with 20 mL of HCl (1 M) twice, and then by the same volume $NaHCO_3$ saturated solution for two times. After, the organic phase was washed once by 20 mL of brine, dried with $MgSO_4$ and filtered. After evaporation of the solvent the crude product was purified by flash chromatography (dichloromethane/hexane, 3:1) to obtain colorless oily product. (616.2 mg, 55 % yield). ^{1}H NMR ($CDCl_3$, 300 MHz) δ(ppm) = 4.30 (t, J = 6.3 Hz, 4H), 3.4 (s, 2H), 2.31 (td, J = 7.0, 2.7 Hz, 4H), 1.99 (t, J = 2.7 Hz, 2H), 1.89 (m, 4H).

T_h-symmetrical C_{60} Hexa(di(pent-4-yn-1-yl)cyclopropane-1,1-dicarboxylate) (2): (Scheme 5). CBr_4 (8.8 g, 26 mmol), compound (**1**) in Scheme S3 (616 mg, 2.6 mmol) and fullerene (187.4 mg, 0.26 mmol) were dissolved in dry toluene (500 mL). DBU (0.78 mL, 5.2 mmol) was introduced into the mixture dropwise. The color of the solution changed from violet to red. The mixture was kept stirring under inert atmosphere for 72 h at room temperature. After that, the organic solution was extracted with 100 mL of saturated $Na_2S_2O_3$ solution, 150 mL of HCl (1 M), deionized water twice, and finally with 100 mL of brine. The organic layer was dried with $MgSO_4$ filtered and concentrated under reduced pressure. The crude product was purified by flash chromatography using dichloromethane as eluting solvent. The product was isolated as orange solid (289.9 mg, 53 % yield). ^{13}C NMR ($CDCl_3$, 75 MHz, Me_4Si) δ (ppm) = 164.0 (*C*=O), 146.1 (sp^2-C C_{60}), 141.4 (sp^2-C C_{60}), 82.8 (*C*≡), 70.2 (*C*H≡), 69.4 (sp^3-C C_{60}), 65.7 (*C*H_2), 45.7 (tert-*C*), 27.5 (*C*H_2), 15.5 (*C*H_2).

6-Azido-hexanoic Acid (3): (Scheme 5) Sodium azide (NaN_3, 1 g, 26 mmol), 6-Bromohexanoic acid (1 g, 5 mmol) and KI (170 mg, 1.02 mmol) were dissolved into deionized H_2O (15 mL) in a 30 mL glass vial. The reaction was carried out in a microwave at 120 °C for 30 min, and cooled down to 55 °C for removing. The mixture was extracted with diethyl ether (20 mL) three times. The organic layer was washed with brine once and dried with $MgSO_4$. A colorless liquid was afforded after concentration at reduced pressure (436 mg, 69 % yield). IR (cm^{-1}): 2090.19 (s, N_3), 1703.23 (s, C=O), 1250.95 (m, C-O). ^{13}C NMR ($CDCl_3$, 175 MHz, Me_4Si) δ (ppm) = 180.3 (*C*=O), 51.5 (N-*C*H_2), 34.1 (*C*H_2), 28.8 (*C*H_2), 26.4 (*C*H_2), 24.4 (*C*H_2).

T_h-symmetrical C_{60} hexa(6,6′-((((cyclopropane-1,1-dicarbonyl)-bis(oxy))bis(propane-3,1-diyl))bis(1H-1,2,3-triazole-4,1-diyl))dihexanoic Acid): (Scheme 5, HF). Compound (Scheme 5 **(2)**) (120 mg, 0.056 mmol) and 6-azido-hexanoic acid (177.2 mg, 1.129 mmol) were dissolved in DMSO (3 mL). Copper bromide dimethyl sulfide complex, CuBr•SMe_2, (81.2 mg, 0.395 mmol) and sodium ascorbate (134.2 mg, 0.677 mmol) were added into the mixture successively. The solution was stirred with a stirrer twined with copper wire under inert atmosphere at room temperature for 48 h. Then, QuadraSil® MP was added to the solution and stirred for 15 min to remove Cu. After filtration the solution was passed through a Sephadex LH-20 column with dichloromethane/methanol (1:1) as elution. The solution was washed by centrifugation

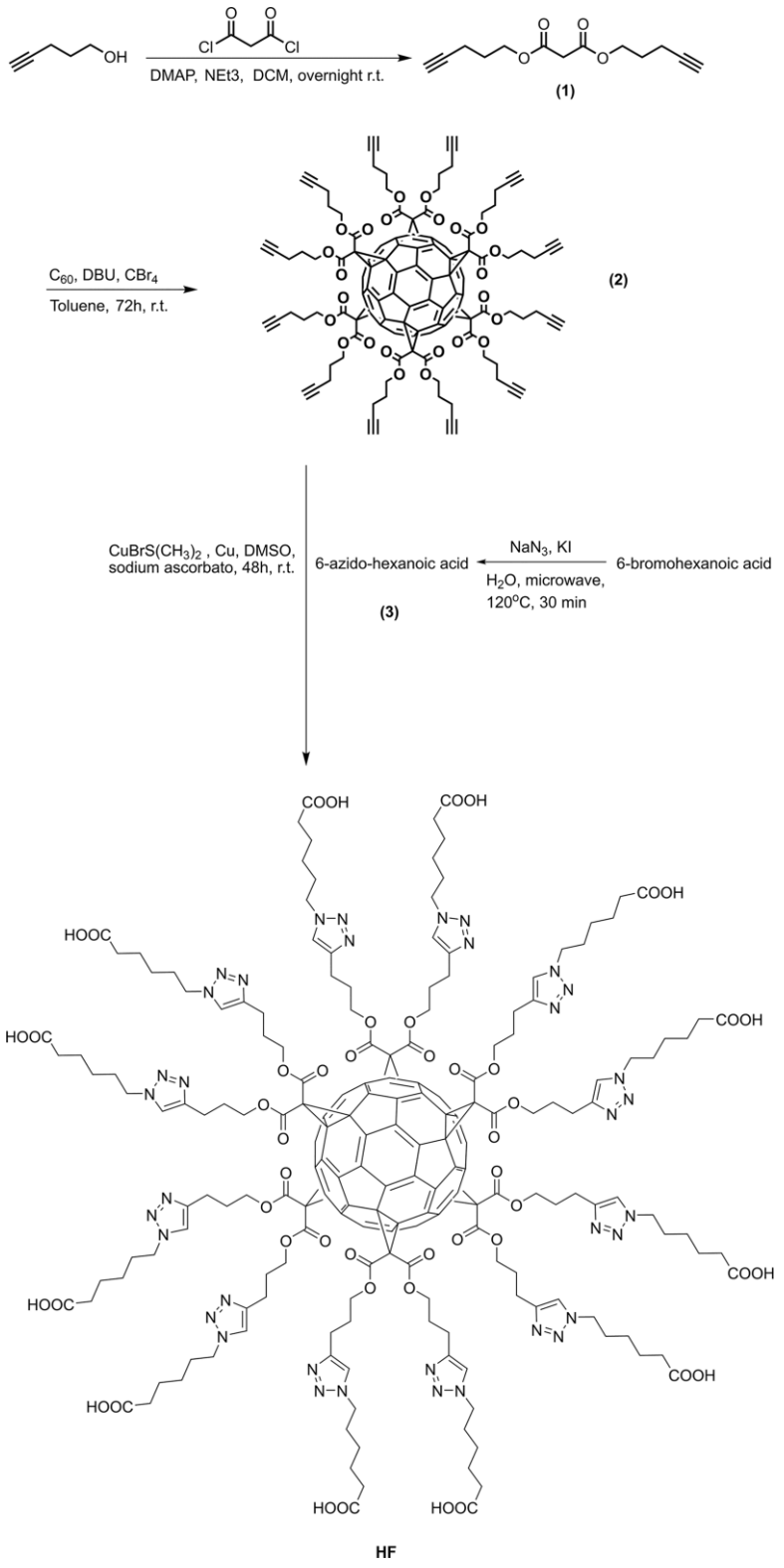

Scheme 5. Synthesis of the hexa-substituted fullerene C_{60} (**HF**) using a Bingel-Hirsch hexaadduct and click chemistry.[51]

with AcOEt (10 min, 6000 rpm) for three times. A dark red solid was isolated (79 mg, 36 % yield). IR (cm^{-1}): 3140 (w, C-H), 1720 (s, C=O), 1459 (w, triazole), 1210 (s, C-O), 1006 (m, C-O). ^{1}H NMR (DMSO, 700 MHz): δ = 12.00 (s, 1H, COOH), 7.89 (s, 1H, N-CH=C), 4.33 (s, 2H, N-CH_2), 4.27 (s, 2H, O-CH2-), 2.63 (s, 2H, CH_2), 2.23 (s, 2H, CH_2), 1.95 (s, 2H, CH_2), 1.77 (s, 2H, CH_2), 1.49 (s, 2H, CH_2), 1.21 (s, 2H, CH_2). ^{13}C NMR (DMSO, 175 MHz, Me_4Si): δ = 207.0 (*C*OOH), 163.3 (*C*=O)145.5 (sp^2-C, C_{60}), 141.2 (sp^2-C, C_{60}), 123.0 (N-*C*H=*C*), 69.2 (sp^3-C, C_{60}), 67.0 (N-CH_2), 49.6 (O-CH_2), 46.0 ppm (tert-*C*), 29.9 (CH_2), 28.2 (CH_2), 26.0 (CH_2), 24.6 (CH_2), 21.8 (CH_2).

Table 3. Calculation of the -COOH/Ru_{surf} ratio.

	Ru_{total}/L	L/Ru_{total}	L/Ru_{surf}	–COOH/Ru_{surf}
Ru@HF	73	0.0137	0.029 (2.2 nm - 47.7 % Ru_{surf})	0.35 (× 12 L/Ru_{surf})
Ru@TPhTC	22.5	0.0444	0.076 (1.7 nm - 58.1 % Ru_{surf})	0.23 (× 3 L/Ru_{surf})

4.4 Synthesis of Ru NP

In a typical experiment, ruthenium precursor [Ru(η^4-C_8H_{12})-(η^6-C_8H_{10})] and the corresponding ligand were dissolved in THF in a Fisher-Porter bottle and the solution was stirred 1 h (30 min for **HF**) at room temperature. After this period of time, 3 bar of dihydrogen were introduced into the bottle. The reaction was allowed to react 16 h at room temperature under vigorous stirring. The excess of H_2 was eliminated and the volume of the solvent was reduced under vacuum. The black solid from the suspension was precipitated after the addition of 200 mL of pentane. After filtration under argon with a cannula, the black solid powder was washed twice with pentane (200 mL) and filtered again before drying under vacuum overnight. For typical ratio and ligand studied, the quantities of the reactants are detailed hereafter:

Ru@TPhC - 10:1: 50 mg (0.159 mmol) of [Ru(η^4-C_8H_{12})(η^6-C_8H_{10})], 13.8 mg (0.0143 mmol) of **TPhC**, and 20 mL of THF. Yield: 21.7 mg.

Ru@TPhTC - 4:1: 200 mg (0.634 mmol) of [Ru(η^4-C_8H_{12})(η^6-C_8H_{10})], 200 mg (0.162 mmol) of **TPhTC**, and 80 mL of THF. Yield: 156.1 mg. Anal.: Ru, 14.4 %.

Ru@TPhTC - 20:1: 200 mg (0.634 mmol) of [Ru(η^4-C_8H_{12})(η^6-C_8H_{10})], 40.6 mg (0.033 mmol) of **TPhTC**, and 80 mL of THF. Yield: 65.7 mg. Anal.: Ru, 50.6 %.

Ru@TPhTC - 40:1: 200 mg (0.634 mmol) of [Ru(η^4-C_8H_{12})(η^6-C_8H_{10})], 20.3 mg (0.016 mmol) of **TPhTC**, and 80 mL of THF. Yield: 81.7 mg. Anal.: Ru, 66.0 %; C, 17.0 %; H, 1.8 %.

Ru@TPhTC - 70:1: 200 mg (0.634 mmol) of [Ru(η^4-C_8H_{12})(η^6-C_8H_{10})], 10.7 mg (0.009 mmol) of **TPhTC**, and 80 mL of THF. Yield: 63.5 mg. Anal: Ru, 66.1 %.

Ru@HF - 120:1: 130 mg (0.412 mmol) of [Ru(η^4-C_8H_{12})(η^6-C_8H_{10})], 13.3 mg (0.0034 mmol) of **HF**, and 2.6 mL of methanol and 26 mL of THF. Yield: 50.4 mg. Anal.: Ru, 65.9 %; C, 16.0 %; H, 1.2 %; N, 2.6 %.

4.5 Catalytic Hydrogenation of Phenylacetylene

In a typical catalytic reaction, a mixture of phenylacetylene (4 mmol, 412 mg), decane (0.5 mmol, 71 mg) and Ru NP catalyst (0.02 mmol of Ru) were dispersed in methanol (25 mL) in a magnetically stirred autoclave with Teflon inner cylinder. The autoclave was purged three times with H_2. The autoclave was pressurized with 5 bar of H_2 at room temperature and stirred at 1500 rpm. Under such conditions, external mass transfer limitation should not be relevant.[15a] The suspension was continuously stirred until the end of the reaction. Gas chromatography (GC) was used to identify the products. After catalysis, samples were taken for TEM analyses, also, the % of Ru on the filtered catalytic solution was ascertained by ICP.

Calculation of Ru Surface Content

The number of Ru atoms in *hcp* cell (N) is 6. Ru atom radius (R_{Ru}) is 0.214 nm. The volume of Ru cell is 0.0817 nm^3. R_{NP} represents the radius of the NP. The volume of all Ru atoms on the shell of NP: $V_{shell} = V_{total} - V_{core} = 4/3\pi R_{NP}^3 - 4/3\pi(R_{NP}-R_{Ru})^3$, V_{total} meaning the volume of one Ru nanoparticle, V_{core} presenting the volume of the NP excluded the one outer layer of atoms. The numbers of Ru atoms on the shell $N_{shell} = N*V_{shell}/0.0817$. The number of total Ru atoms $N_{total} = N*V_{total}/0.0817$. The percentage of Ru atoms on the surface of the NP = $N_{shell}/N_{total}*100$ %. For calculation of the COOH/Ru_{surf} ratio see Table 3.

Acknowledgments

We acknowledge the Centre National de la Recherche Scientifique (CNRS) and Institute Nationale Polytechnique (INP). This work was supported by the Agence Nationale de la Recherche (ANR project ANR-16-CE07-0007-01, Icare-1), which is gratefully acknowledged.

Keywords: Metallic nanoparticles · Ruthenium · Covalent assembly · Acetylene hydrogenation · Confinement effect

[1] A. Küchler, M. Yoshimoto, S. Luginbühl, F. Mavelli, P. Walde, *Nat. Nanotechnol.* **2016**, *11*, 409–420.
[2] a) S. Sadjadi in *Organic Nanoreactors* (Ed.: S. Sadjadi), Academic Press, Boston, **2016**, pp. 1–14; b) P. Ballester, *Angew. Chem. Int. Ed.* **2017**, *56*, 7713; *Angew. Chem.* **2017**, *56*, 7713–7714.
[3] a) S. H. Petrosko, R. Johnson, H. White, C. A. Mirkin, *J. Am. Chem. Soc.* **2016**, *138*, 7443–7445; b) M. T. De Martino, L. K. E. A. Abdelmohsen, F. P. J. T. Rutjes, J. C. M. van Hest, *Beilstein J. Org. Chem.* **2018**, *14*, 716–733.
[4] a) F. Yang, D. Deng, X. Pan, Q. Fu, X. Bao, *Natl. Sci. Rev.* **2015**, *2*, 183–201; b) F. Goettmann, C. Sanchez, *J. Mater. Chem.* **2007**, *17*, 24–30; c) V. Mouarrawis, R. Plessius, J. I. van der Vlugt, J. N. H. Reek, *Front. Chem.* **2018**, *6*, 623.
[5] B. Smit, T. L. M. Maesen, *Nature* **2008**, *451*, 671–678.
[6] W. Sparreboom, A. van den Berg, J. C. T. Eijkel, *New J. Phys.* **2010**, *12*, 015004.
[7] L. D. Gelb, K. E. Gubbins, R. Radhakrishnan, M. Sliwinska-Bartkowiak, *Rep. Prog. Phys.* **2000**, *63*, 727–727.
[8] C. Alba-Simionesco, B. Coasne, G. Dosseh, G. Dudziak, K. E. Gubbins, R. Radhakrishnan, M. Sliwinska-Bartkowiak, *J. Phys. Condens. Matter* **2006**, *18*, R15–R68.
[9] Y. Long, J. C. Palmer, B. Coasne, M. Śliwinska-Bartkowiak, K. E. Gubbins, *Phys. Chem. Chem. Phys.* **2011**, *13*, 17163–17170.
[10] a) S.-M. Wu, X.-Y. Yang, C. Janiak, *Angew. Chem. Int. Ed.* **2019**, *131*, 12468; *Angew. Chem.* **2019**, *58*, 12340–12354; b) N. Kosinov, C. Liu, E. J. M. Hensen, E. A. Pidko, *Chem. Mater.* **2018**, *30*, 3177–3198; c) G. Sastre, A. Corma, *J. Mol. Catal. A* **2009**, *305*, 3–7.
[11] a) N. Wang, Q. Sun, J. Yu, *Adv. Mater.* **2019**, *31*, 1803966; b) Q. Yang, Q. Xu, H.-L. Jiang, *Chem. Soc. Rev.* **2017**, *46*, 4774–4808.
[12] a) P. Serp, E. Castillejos, *ChemCatChem* **2010**, *2*, 41–47; b) S. A. Miners, G. A. Rance, A. N. Khlobystov, *Chem. Soc. Rev.* **2016**, *45*, 4727–4746.
[13] S. Lu, Y. Hu, S. Wan, R. McCaffrey, Y. Jin, H. Gu, W. Zhang, *J. Am. Chem. Soc.* **2017**, *139*, 17082–17088.
[14] a) H. Li, J. Xiao, Q. Fu, X. Bao, *Proc. Natl. Acad. Sci. USA* **2017**, *114*, 5930–5934; b) L. Tang, X. Meng, D. Deng, X. Bao, *Adv. Mater.* **2019**, *31*, 1901996.
[15] a) Y. Min, M. R. Axet, P. Serp, in *Molecular Catalysis* (Eds.: P. W. N. M. van Leeuwen, C. Claver), Springer Nature, Switzerland AG **2020**, vol. 1, pp. 129–198; b) Y. Min, H. Nasrallah, D. Poinsot, P. Lecante, Y. Tison, H. Martinez, P. Roblin, A. Falqui, R. Poteau, I. del Rosal, I. C. Gerber, J.-C. Hierso, M. R. Axet, P. Serp, *Chem. Mater.* **2020**, *32*, 2365–2378; c) F. Leng, I. C. Gerber, P. Lecante, A. Bentaleb, A. Muñoz, B. M. Illescas, N. Martín, G. Melinte, O. Ersen, H. Martinez, *Chem. Eur. J.* **2017**, *23*, 13379–13386; d) T. Huang, G. Sheng, P. Manchanda, A. H. Emwas, Z. Lai, S. P. Nunes, K.-V. Peinemann, *Sci. Adv.* **2019**, *5*, eaax6976.
[16] N. Marro, F. della Sala, E. R. Kay, *Chem. Sci.* **2020**, *11*, 372–383.

[17] M. K. Kinnan, G. Chumanov, *J. Phys. Chem. C* **2010**, *114*, 7496–7501.
[18] R. Li, X. Zhu, D. Shou, X. Zhou, X. Yan, *RSC Adv.* **2016**, *6*, 88486–88489.
[19] a) S. Julin, S. Nummelin, M. A. Kostiainen, V. Linko, *J. Nanopart. Res.* **2018**, *20*, 119; b) C. George, I. Szleifer, M. Ratner, *ACS Nano* **2013**, *7*, 108–116; c) I. Fratoddi, R. Matassa, L. Fontana, I. Venditti, G. Familiari, C. Battocchio, E. Magnano, S. Nappini, G. Leahu, A. Belardini, R. Li Voti, C. Sibilia, *J. Phys. Chem. C* **2017**, *121*, 18110–18119; d) S. K. Ghosh, T. Pal, *Chem. Rev.* **2007**, *107*, 4797–4862.
[20] S. Sreedhala, C. P. Vinod, *Chem. Commun.* **2015**, *51*, 10178–10181.
[21] E. Morsbach, S. Kunz, M. Bäumer, *Catal. Sci. Technol.* **2016**, *6*, 339–348.
[22] a) H. Yan, S. I. Lim, Y.-J. Zhang, Q. Chen, D. Mott, W.-T. Wu, D.-L. An, S. Zhou, C.-J. Zhong, *Chem. Commun.* **2010**, *46*, 2218–2220; b) WangWang, X. Shi, N. N. Kariuki, M. Schadt, G. R. Wang, Q. Rendeng, J. Choi, J. Luo, S. Lu, C.-J. Zhong, *J. Am. Chem. Soc.* **2007**, *129*, 2161–2170; c) R. Abargues, S. Albert, J. L. Valdés, K. Abderrafi, J. P. Martínez-Pastor, *J. Mater. Chem.* **2012**, *22*, 22204–22211.
[23] a) S. Kumar, *Liq. Cryst.* **2004**, *31*, 1037–1059; b) S. K. Pal, S. Setia, B. S. Avinash, S. Kumar, *Liq. Cryst.* **2013**, *40*, 1769–1816.
[24] a) D. Sonet, B. Bibal, *Tetrahedron Lett.* **2019**, *60*, 872–884; b) L.-P. Yang, C.-Y. Pan, *Macromol. Chem. Phys.* **2008**, *209*, 783–793; c) C. T. Kresge, M. E. Leonowicz, W. J. Roth, J. C. Vartuli, J. S. Beck, *Nature* **1992**, *359*, 710–712; d) C. D. Sheraw, L. Zhou, J. R. Huang, D. J. Gundlach, T. N. Jackson, M. G. Kane, I. G. Hill, M. S. Hammond, J. Campi, B. K. Greening, J. Francl, J. West, *Appl. Phys. Lett.* **2002**, *80*, 1088–1090; e) S. Das, F. Irin, H. S. Tanvir Ahmed, A. B. Cortinas, A. S. Wajid, D. Parviz, A. F. Jankowski, M. Kato, M. J. Green, *Polymer* **2012**, *53*, 2485–2494.
[25] a) A. Mahringer, A. C. Jakowetz, J. M. Rotter, B. J. Bohn, J. K. Stolarczyk, J. Feldmann, T. Bein, D. D. Medina, *ACS Nano* **2019**, *13*, 6711–6719; b) E. M. Miner, L. Wang, M. Dinca, *Chem. Sci.* **2018**, *9*, 6286–6291; c) L. Yang, X. He, M. Dinca, *J. Am. Chem. Soc.* **2019**, *141*, 10475–10480.
[26] M. Mansueto, S. Sauer, M. Butschies, M. Kaller, A. Baro, R. Woerner, N. H. Hansen, G. Tovar, J. Pflaum, S. Laschat, *Langmuir* **2012**, *28*, 8399–8407.
[27] a) Z. Shen, M. Yamada, M. Miyake, *J. Am. Chem. Soc.* **2007**, *129*, 14271–14280; b) A. Gowda, S. Kumar, *Materials* **2018**, *11*, 382.
[28] M. Hara, S. Nagano, T. Seki, *J. Am. Chem. Soc.* **2010**, *132*, 13654–13656.
[29] a) D. P. Dinega, M. Bawendi, *Angew. Chem. Int. Ed.* **1999**, *38*, 1788–1791; *Angew. Chem.* **1999**, *111*, 1906; b) F. Dassenoy, M.-J. Casanove, P. Lecante, M. Verelst, E. Snoeck, A. Mosset, T. O. Ely, C. Amiens, B. Chaudret, *J. Chem. Phys.* **2000**, *112*, 8137–8145.
[30] a) O. Margeat, M. Respaud, C. Amiens, P. Lecante, B. Chaudret, *Beilstein J. Nanotechnol.* **2010**, *1*, 108–118; b) E. Bonnefille, F. Novio, T. Gutmann, R. Poteau, P. Lecante, J.-C. Jumas, K. Philippot, B. Chaudret, *Nanoscale* **2014**, *6*, 9806–9816; c) R. Choukroun, D. de Caro, B. Chaudret, P. Lecante, E. Snoeck, *New J. Chem.* **2001**, *25*, 525–527.
[31] R. Mas-Balleste, C. Gomez-Navarro, J. Gomez-Herrero, F. Zamora, *Nanoscale* **2011**, *3*, 20–30.
[32] R. Besselink, T. Stawski, A. Van Driessche, L. G. Benning, *J. Chem. Phys.* **2016**, *145*, 211908.
[33] B. F. Machado, M. Oubenali, M. Rosa Axet, T. Trang Nguyen, M. Tunckol, M. Girleanu, O. Ersen, I. C. Gerber, P. Serp, *J. Catal.* **2014**, *309*, 185–198.
[34] R. Gonzalez-Gomez, L. Cusinato, C. Bijani, Y. Coppel, P. Lecante, C. Amiens, I. del Rosal, K. Philippot, R. Poteau, *Nanoscale* **2019**, *11*, 9392–9409.
[35] P. Uznanski, J. Zakrzewska, F. Favier, S. Kazmierski, E. Bryszewska, *J. Nanopart. Res.* **2017**, *19*, 121.
[36] E. Bresó-Femenia, B. Chaudret, S. Castillón, *Catal. Sci. Technol.* **2015**, *5*, 2741–2751.
[37] N. Chakroune, G. Viau, S. Ammar, L. Poul, D. Veautier, M. M. Chehimi, C. Mangeney, F. Villain, F. Fievet, *Langmuir* **2005**, *21*, 6788–6796.
[38] a) H. Li, Q. Zheng, C. Han, *Analyst* **2010**, *135*, 1360–1364; b) V. Kamalraj, S. Senthil, P. Kannan, *J. Mol. Struct.* **2008**, *892*, 210–215.
[39] V. Krishnakumar, R. J. Xavier, *Spectrochim. Acta Part A* **2004**, *60*, 709–714.
[40] *United States Pat.,* 6,727,398, **2004**.
[41] M. Bystrzanowska, P. Petkov, M. Tobiszewski, *ACS Sustainable Chem. Eng.* **2019**, *7*, 18434–18443.
[42] M. R. Axet, K. Philippot, *Chem. Rev.* **2020**, *120*, 1085–1145.
[43] a) W. Qian, L. Lin, Y. Qiao, X. Zhao, Z. Xu, H. Gong, D. Li, M. Chen, R. Huang, Z. Hou, *Appl. Catal. A* **2019**, *585*, 117183; b) S. Noël, D. Bourbiaux, N. Tabary, A. Ponchel, B. Martel, E. Monflier, B. Léger, *Catal. Sci. Technol.* **2017**, *7*, 5982–5992; c) L. Rakers, L. M. Martinez-Prieto, A. M. Lopez-Vinasco, K. Philippot, P. van Leeuwen, B. Chaudret, F. Glorius, *Chem. Commun.* **2018**, *54*, 7070–7073; d) C. Li, Z. Shao, M. Pang, C. T. Williams, X. Zhang, C. Liang, *Ind. Eng. Chem. Res.* **2012**, *51*, 4934–4941; e) M. Dhiman, B. Chalke, V. Polshettiwar, *ACS Sustainable Chem. Eng.* **2015**, *3*, 3224–3230; f) J.-Y. Ruzicka, D. P. Anderson, S. Gaw, V. B. Golovko, *Aust. J. Chem.* **2012**, *65*, 1420–1425; g) T. López, J. Hernandez-Ventura, M. Asomoza, A. Campero, R. Gómez, *Mater. Lett.* **1999**, *41*, 309–316; h) A. Maximov, A. Zolotukhina, L. Kulikov, Y. Kardasheva, E. Karakhanov, *React. Kinet. Mech. Catal.* **2016**, *117*, 729–743; i) M. Niu, Y. Wang, W. Li, J. Jiang, Z. Jin, *Catal. Commun.* **2013**, *38*, 77–81; j) S. Ji, Y. Chen, S. Zhao, W. Chen, L. Shi, Y. Wang, J. Dong, Z. Li, F. Li, C. Chen, Q. Peng, J. Li, D. Wang, Y. Li, *Angew. Chem. Int. Ed.* **2019**, *58*, 4271–4275; *Angew. Chem.* **2019**, *131*, 4315.
[44] S. Domínguez-Domínguez, Á. Berenguer-Murcia, B. K. Pradhan, Á. Linares-Solano, D. Cazorla-Amorós, *J. Phys. Chem. C* **2008**, *112*, 3827–3834.
[45] a) M. J.-L. Tschan, O. Diebolt, P. W. N. M. van Leeuwen, *Top. Catal.* **2014**, *57*, 1054–1065; b) S. Campisi, M. Schiavoni, C. E. Chan-Thaw, A. Villa, *Catalysts* **2016**, *6*, 185; c) L. M. Rossi, J. L. Fiorio, M. A. S. Garcia, C. P. Ferraz, *Dalton Trans.* **2018**, *47*, 5889–5915.
[46] a) N. Tiengchad, O. Mekasuwandumrong, C. Na-Chiangmai, P. Weerachawanasak, J. Panpranot, *Catal. Commun.* **2011**, *12*, 910–916; b) H. Tian, F. Huang, Y. Zhu, S. Liu, Y. Han, M. Jaroniec, Q. Yang, H. Liu, G. Qing, M. Lu, J. Liu, *Adv. Funct. Mater.* **2018**, *28*, 1801737; c) L. Xia, D. Li, J. Long, F. Huang, L. Yang, Y. Guo, Z. Jia, J. Xiao, H. Liu, *Carbon* **2019**, *145*, 47–52; d) J. Tang, P. Liu, X. Liu, L. Chen, H. Wen, Y. Zhou, J. Wang, *ACS Appl. Mater. Interfaces* **2020**, *12*, 11522–11532.
[47] S. K. Kaiser, R. Lin, F. Krumeich, O. V. Safonova, J. Pérez-Ramírez, *Angew. Chem. Int. Ed.* **2019**, *58*, 12297–12304; *Angew. Chem.* **2019**, *58*, 12297–12304.
[48] B. Feringán, P. Romero, J. L. Serrano, C. L. Folcia, J. Etxebarria, J. Ortega, R. Termine, A. Golemme, R. Giménez, T. Sierra, *J. Am. Chem. Soc.* **2016**, *138*, 12511–12518.
[49] Z. Ke-Qing, W. Bi-Qin, H. Ping, L. Quan, Z. Liang-Fu, *Chin. J. Chem.* **2005**, *23*, 767–774.
[50] W. Xiao, Z. He, M. Xu, N. Wu, X. Kong, X. Jing, *Tetrahedron Lett.* **2015**, *56*, 700–705.
[51] a) J. Iehl, R. Pereira de Freitas, B. Delavaux-Nicot, J. F. Nierengarten, *Chem. Commun.* **2008**, 2450–2452; b) A. Hirsch, O. Vostrowsky, *Eur. J. Org. Chem.* **2001**, *2001*, 829–848; c) M. Sanchez-Navarro, A. Munoz, B. M. Illescas, J. Rojo, N. Martin, *Chem. Eur. J.* **2011**, *17*, 766–769.